ACS Photonics

pubs.acs.org/journal/apchd5

Article

1D Self-Healing Beams in Integrated Silicon Photonics

Zhuoran Fang,* Rui Chen, Albert Ryou, and Arka Majumdar*

Cite This: https://doi.org/10.1021/acsphotonics.1c00581

Read Online

ACCESS | Metrics & More | Article Recommendations | Supporting Information

ABSTRACT: Since the first experimental observation of optical Airy beams, various applications ranging from particle and cell micromanipulation to laser micromachining have exploited their nondiffracting and accelerating properties. The later discovery that Airy beams can self-heal after being blocked by an obstacle further proved their robustness to propagate under a scattering and disordered environment. Here, we report the generation of an Airy-like accelerating beam on an integrated silicon photonic chip and demonstrate that the on-chip 1D Airy-like accelerating beams preserve the same properties as the 2D Airy beams. The 1D synthetic-phase meta-optics used to create the accelerating beam has the size of only 3 μm × 16 μm, at least 3 orders of magnitude smaller than the conventional optic. The on-chip self-healing beams demonstrated here could potentially enable diffraction-free light routing for on-chip optical networks and high-precision micromanipulation of biomolecules on an integrated photonic chip.

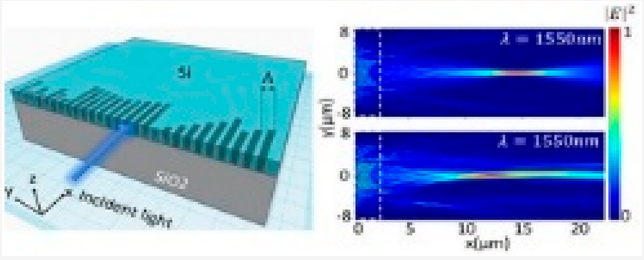

KEYWORDS: *silicon photonics, meta-optics, accelerating beams, laser beam shaping*

Nondiffracting beams, exemplified by the well-known Bessel beam,[1] have long been pursued in the photonics community to avoid the ubiquitous phenomenon of diffraction in Gaussian beams. In practice, these "non-spreading" beams are normally truncated by an aperture, so they do tend to diffract during propagation.[2] However, by using an appropriate size of the aperture, the diffraction can be significantly slowed down over the intended propagation distance, and for many practical applications, they can be considered "diffraction-free". Unlike the straight propagating Bessel beams, Airy beams emerge as an alternative nondiffracting solution to the paraxial wave equation that exhibits parabolic trajectory during propagation.[3] Airy beams were first predicted and experimentally observed in the optical domain by Siviloglou and Christodoulides[2,4] and subsequently demonstrated in electrons[5] and plasmons.[6] It was soon discovered that Airy beams can reconstruct themselves after being blocked by an obstacle or propagating through a turbulent environment.[7] Following these experimental observations, numerous works have exploited the nondiffracting, self-bending, and self-healing properties of Airy beams for applications in microscopy,[8,9] particle and cell manipulation,[10−12] optical trapping,[12] micro- and nano machining,[13,14] and optical filamentation.[15,16]

Traditionally, Airy beams are generated by reflecting light from a cubic phase mask, usually realized by a spatial light modulator (SLM), and then focused by a spherical lens in free space. It was later shown that an approximated version of Airy beam can also be generated by directly imparting a 3/2 phase profile on the Gaussian beam which significantly reduces the system length since no external lens is required.[17−19] However, the SLMs that are used to implement the phase profile tend to be extremely bulky and have large pixel and pitch size (typically 10× the wavelength of light) that only allows limited resolution in phase discretization. Hence, the use of SLMs is not desirable for miniaturization and high-density integration. To further reduce the dimensions of the optics, Zhan et al. has proposed to combine the quadratic and cubic phase function in one single ultrathin SiN metasurface, which can generate Airy-shaped beams in free-space without SLMs. Such a synthetic-phase metasurface[20] was also adopted in a recent work to generate a 2D Airy beam with controlled focal length, beam width, and extended propagation distance. Yet, precise alignment of the complex optical setup is still required, which adds difficulty to the experiments and precludes the miniaturization of the whole optical system. In this paper, we demonstrate for the first time the generation of self-healing Airy-like accelerating beams in integrated silicon photonics near the telecommunication wavelength using an on-chip synthetic-phase meta-optic. We show that the 1D on-chip Airy-like beams preserve the nondiffracting and self-healing properties of 2D Airy beams. The on-chip synthetic-phase meta-optic used to generate the 1D accelerating beams has the size of 3 μm × 16 μm, which is almost 3 orders of magnitude smaller than the conventional macroscopic optics. Furthermore, no alignment of optical components is required as the

Received: April 18, 2021

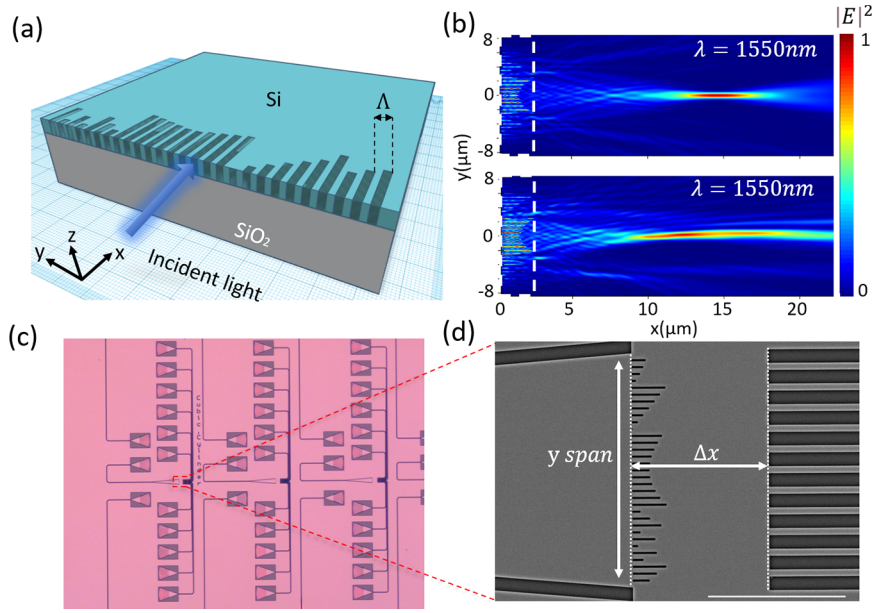

Figure 1. Design of on-chip synthetic-phase meta-optics. (a) Schematic showing the structure of 1D synthetic-phase meta-optics. The blue arrow indicates the direction in which the light is launched into the metalens. (b) Simulated electric field intensity of light focused by a quadratic meta-optics (top) and synthetic-phase meta-optics (bottom). The focal length is 15 μm for both metasurfaces, and α of the synthetic-phase meta-optics is 0.025. The white dashed boxes highlight where the phase masks are. (c) Optica micrograph showing three synthetic-phase meta-optics of increasing Δx. Grating couplers that are used to extract the light intensity at each port are also visible. (d) SEM image of a synthetic-phase meta-optics on SOI (scale bar: 10 μm).

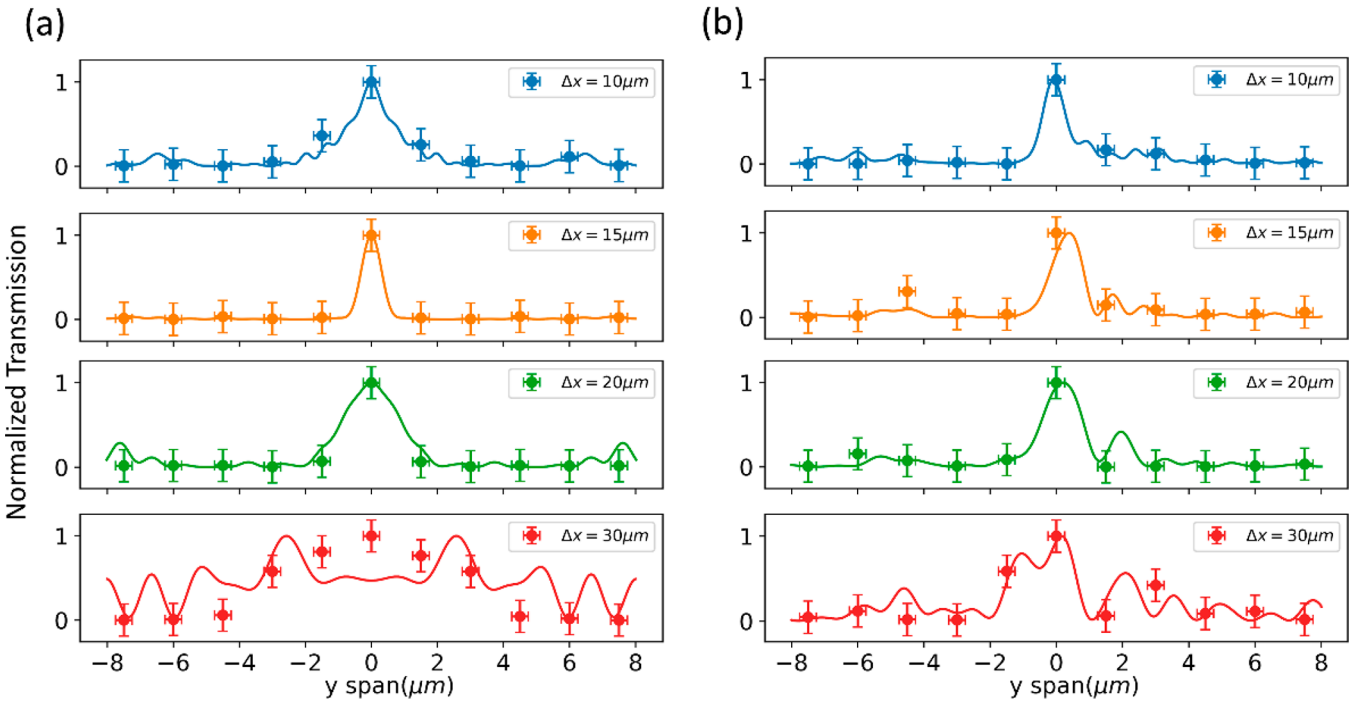

Figure 2. Experimental results of 1D nondiffracting accelerating beam. (a) Intensity distribution across the y span of light focused by a quadratic metalens. Optical transmission is measured at Δx = 10, 15, 20, and 30 μm. (b) Intensity distribution across the y span of light focused by a synthetic-phase meta-optic. Optical transmission is measured at Δx = 10, 15, 20, and 30 μm. Solid lines are the simulation results and dots are the measured data in experiment at each waveguide. Error bars in x are determined by the lateral span of the intensity point, which equals to the 500 nm waveguide width. Error bars in y are calculated from the standard deviation of grating coupler efficiency across the whole chip.

meta-optics combine the functionality of a cubic phase-mask and the lens in a single device. The integrated synthetic-phase meta-optics can provide alignment with other optical components on-chip with nanometer scale precision controlled by the lithography. Finally, we showed that the on-chip Airy-shaped beam can self-heal, which can provide a way to efficiently route light in the presence of fabrication imperfections and will be beneficial for large-scale on-chip optical interconnects. Future applications of our on-chip accelerating beams include 1 × N switches for on-chip light

https://doi.org/10.1021/acsphotonics.1c00581
ACS Photonics XXXX, XXX, XXX−XXX

routing,[21,22] high precision optical trapping,[12,23] and particle manipulation[10] on a chip.

RESULTS

Drawing on the design principle proposed by Wang[24] and Zhan,[25] we incorporate the cubic phase mask into the quadratic lens phase mask to generate 1D Airy-like beams using a 1D synthetic-phase function:

$$\phi(y) = \frac{2\pi}{\lambda} n_{\text{eff}}(f - \sqrt{f^2 + y^2}) + \alpha y^3 \quad (1)$$

where λ is the operating wavelength, n_{eff} is the effective index of silicon-on-insulator (SOI) waveguide, f is the focal length of the 1D metalens, y is the lateral extent of the meta-optics, and α controls the strength of the cubic term relative to the quadratic term. Such a synthetic phase profile can be readily implemented by tuning the length of the air slot etched into the silicon slab (Figure 1a) on silicon dioxide. A focal length of 15 μm is chosen to provide a good trade-off between the focusing efficiency and the collected light intensity. The range over which the accelerating beam profile appears, also known as the depth of focus, can be controlled by adjusting α: increasing α increases the depth of focus as the cubic phase becomes more dominant. However, a larger α will also lead to a broader main lobe and increased side lobes (Supporting Information, Figure S1), which compromises the efficiency of the meta-optics since a focused main lobe is generally desired for most practical applications.[10−12] For example, at α = 0.025 the accelerating beam stays focused from Δx = 10−20 μm but becomes broad and exhibits multiple side lobes across the same range at α = 0.1 (Supporting Information, Figure S1), Δx being the distance between the input and output ports, as shown in Figure 1d. Here, α is chosen to be 0.025 to ensure that the depth of focus includes the focal point (Δx = 15 μm) and the main lobe intensity of the Airy-like beam is large, since the underlying Gaussian beam is also focused in the same range. This is particularly important for experimental measurements, as stronger light intensity ensures higher signal-to-noise ratio. Figure 1b compares the simulated 2D intensity profile of the light propagating through the quadratic (top) and 1D synthetic-phase meta-optics (bottom) at 1550 nm. The pitch Λ, as indicated in Figure 1a, is chosen to be 500 nm, and the duty cycle η (defined as $\eta = \frac{w}{\Lambda}$, where w is the width of the air slot) is 0.215 for both meta-optics, ensuring high transmission through the air slot.[24] For this combination of Λ and η, n_{eff} is calculated to be 2.18 using the finite difference time domain (FDTD) simulation. The quadratic metalens implements only the quadratic part of the phase mask defined by eq 1, while the synthetic-phase meta-optics implements the whole phase. Light is focused by the quadratic metalens at around Δx = 15 μm but quickly diverges. On the other hand, the synthetic-phase meta-optics produces a curved beam with an extended depth of focus (EDOF), a defining signature of an accelerating beam (Figure 1b).

The simulation is experimentally verified using an integrated silicon photonic chip (see Methods for fabrication details), and the results are shown in Figure 2. Figure 2a and b compares the 1D intensity distribution of light propagating different distances of Δx from a quadratic metalens and a synthetic-phase meta-optic, respectively. The experimental data is overlaid on the simulation result (the solid line). We emphasize that no fitting was used in the solid line except a global normalization. The simulated data is obtained using a FDTD simulation, and no assumption on any particular beam profile was made. The optical transmission is collected across the y span of the meta-optics using a vertical fiber setup via multiple waveguides (indicated in Figure 1d; see Methods for experimental setup). A typical Gaussian beam profile can be seen from Figure 2a, matching the simulation. The beam focuses tightly near Δx = 15 μm (fwhm ∼ 0.7 μm), begins to diverge at Δx = 20 μm, and diverges remarkably at Δx = 30 μm (fwhm ∼ 6 μm). In contrast, the beam originating from the synthetic-phase meta-optics maintains a narrow fwhm of ∼1 μm across the same propagation distance (Figure 2b), particularly at Δx = 30 μm, where the Gaussian beam diverges significantly and becomes very broad (see also Figure S2 in the Supporting Information). The asymmetric beam profile and the formation of side lobes in Figure 2b are characteristics of accelerating beams. Furthermore, an interesting phenomenon is observed at Δx = 30 μm, where a secondary lobe at $y \sim -1$ μm starts to form next to the main lobe. We found in simulation that this secondary lobe will gradually split from the main lobe and subsequently evolves into the main lobe as the beam propagates. Such a phenomenon is also observed in the 2D Airy beam generated by a synthetic-phase metasurface[20] at long propagation distances. Future work will be required to investigate the theory behind it and whether this phenomenon is universal in the accelerating beam generated from a synthetic-phase metasurface. Although the 1D accelerating beam is not as tightly focused as the Gaussian beam at the focal length, it exhibits a moderately intense beam across a wider range. This could be beneficial for beam routing applications where different wavelengths of light or objects at different locations along the optical axis can be equally focused by the meta-optics, as exploited for imaging via a 2D Airy-like beam.[26] Note that the experimental results at Δx = 30 μm for quadratic metalens (Figure 2a) deviate more from the simulation than the results for accelerating beam (Figure 2b). We primarily attribute this to the significant increase of side lobes from the stronger diffraction of Gaussian beam. The limited resolution of output ports determined by the waveguide spacings (1.5 μm), which is stipulated by the 1.55 μm operating wavelength to avoid cross talk between waveguides, fails to capture the multiple diffraction lobes accurately. Additionally, the reduction of the signal-to-noise ratio could also contribute to the inaccuracy. In fact, we found in experiments that the light intensity of the Gaussian main lobe drops to approximately 60% of that of the accelerating beam main lobe at Δx = 30 μm. Nevertheless, we clearly observe the nondiffracting nature of the 1D accelerating beam.

The error bars in the x-axis of Figure 2 are determined by the lateral span of each waveguide (∼500 nm). Each waveguide (as shown in Figure 1c,d) is connected to its own grating coupler that gives one data point. Hence, even for the same plane along the optical axis, each data point is collected from several different grating couplers. Due to fabrication imperfections, different grating couplers will have different outcoupling efficiencies. Hence, although the intensity in one plane is normalized, the local variation of the grating coupler efficiency will still give errors to the overall intensity distribution. Such efficiency variation can be significant due to the nonuniform etching across the sample and local perturbation from bubbles trapped inside the resist, which cannot be taken into account purely from normalization. This variation (estimated by measuring 36 pairs of grating coupler

https://doi.org/10.1021/acsphotonics.1c00581
ACS Photonics XXXX, XXX, XXX−XXX

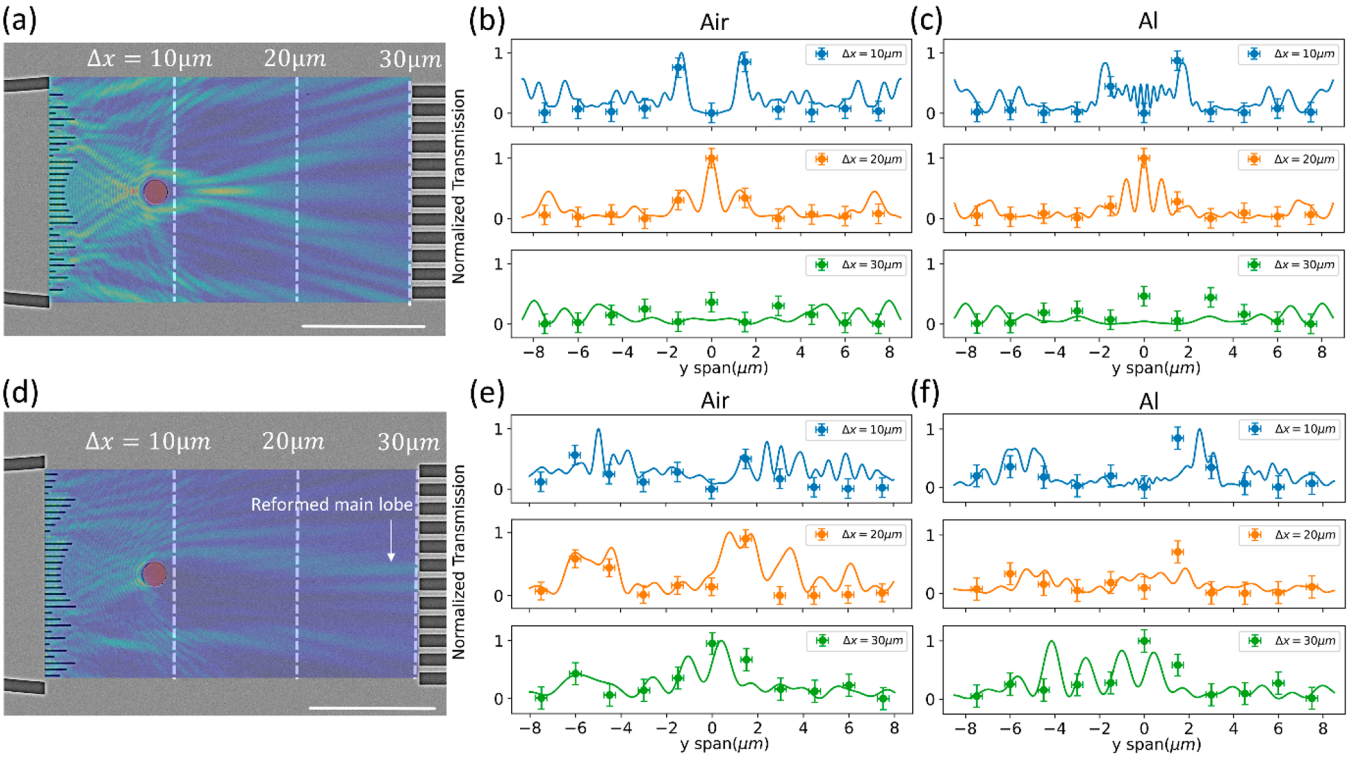

Figure 3. Self-healing of on-chip 1D accelerating beam. (a) SEM showing the quadratic metalens and the circular air pocket (scale bar: 10 μm). The scatterer is highlighted with false color and the simulated electric field distribution is overlapped onto the SEM image. The white dashed lines indicate where the optical transmission is measured. (b) Intensity distribution across the y span showing the scattering of Gaussian beam by a circular air hole. (c) Intensity distribution across the y span showing the scattering of Gaussian beam by a circular Al scatterer. (d) SEM showing the synthetic-phase meta-optic and the circular air pocket (scale bar: 10 μm). The reformed Airy-like main lobe is indicated by an arrow. (e) Intensity distribution across the y span showing the scattering of Airy-like beam by a circular air pocket. (f) Intensity distribution across the y span showing the scattering of Airy-like beam by a circular Al scatterer. Solid lines are the simulation results and dots are the measured data in experiment at each waveguide. Error bars in x are determined by the lateral span of the intensity point which equals to the 500 nm waveguide width. Error bars in y are calculated from the standard deviation of grating coupler efficiency across the whole chip.

across the same chip) determines the error bar in the y-axis in Figure 2. We have also characterized the noise from our fiber setup, including the detector, by measuring the transmission from a waveguide for 10 min. The noise is found to be less than ±0.5 dBm. Such noise level when plotted as error bars will not even be visible when compared to the efficiency variation from the grating couplers, which is around a few dBs. Hence, we can safely neglect the noise from the fiber and detector and attribute the intensity variation purely to the nonuniformity in grating couplers.

We then experimentally verify the self-healing properties of the Airy-like beam (see Figure 3). Here, a circular air pocket (centered at Δx = 8.8 μm, y = 0 μm) of 1 μm radius is used to scatter the main lobes of the Gaussian beam and Airy-shaped beam, as shown in Figure 3a and 3d, respectively. The position of the air pocket is based on the position where we first observed the Gaussian or Airy beam profile, which is at 10 μm, as shown in Figure 2. We place the scatterer at 8.8 μm to ensure the main lobe is completely suppressed at 10 μm, since the air pocket is 1 μm in radius. By doing this we can easily compare the unperturbed and perturbed beam profile at the same propagation distance and confirm that the beam is indeed blocked before the self-healing can happen (200 nm is too short for the beam to self-heal). In real devices, the position of the scatterer will be random, and the scatterer will unlikely block the entire main lobe. Our experiment aims to simulate the most extreme condition where the main lobe is completely suppressed by the scatterer when the beam just starts to form. Optical transmission is measured at Δx = 10, 20, and 30 μm where the position and size of the scatterer is fixed. The simulated 2D electric field profile is superimposed on the SEMs of the meta-optics along with the scatterers. Strong scattering occurs as the Gaussian beam interacts with the air pocket, forming multiple symmetric side lobes (Figure 3a). The beam scatters around the air cylinder and focuses again but the intensity deteriorates dramatically compared to Figure 1b. At Δx = 30 μm, the main lobe of the Gaussian beam becomes almost indistinguishable as most energy scatters into the side lobes. This phenomenon is also observed experimentally for both air and aluminum scatterer shown in Figure 3b,c. The Gaussian main peak is completely suppressed at Δx = 10 μm and partially reforms with multiple side peaks at Δx = 20 μm. At Δx = 30 μm, the energy in the main lobe is completely transferred to the low-intensity side lobes due to the strong scattering. Replacing the air scatterer with aluminum yields similar results (Figure 3c). On the other hand, the synthetic-phase meta-optic produces beams that are scattered less prominently by the same air pocket (Figure 3d), because the intensity of the accelerating beam is distributed more uniformly along the transverse direction. It can be clearly seen from the electric filed profile in Figure 3d that the side lobes not blocked by the air pocket reform the main lobe after propagation over a certain distance, as indicated by the white arrow. This phenomenon matches the underlying principle of

https://doi.org/10.1021/acsphotonics.1c00581
ACS Photonics XXXX, XXX, XXX−XXX

self-healing of Airy beams.[10,27] Distinct rays contribute to the main lobes at different propagation distances. When the main lobe is blocked, the unblocked rays from the side lobes will reconstitute the main lobe after a "healing distance".[7] The experimental data in Figure 3e shows that at Δx = 10 μm, the main lobe is completely blocked whereas the side lobes are not. The side lobes become more intense and merge to form the main lobe at Δx = 20 μm as the self-healing gradually takes place. At Δx = 30 μm, the main lobe reforms completely when the maxima re-emerges at the center y = 0 μm (see also Figure S3 in the Supporting Information). Figure 3f shows the experimental results of 1D accelerating beam being blocked by an Al scatterer. Since almost no light from the main lobe is able to penetrate the metal, the side lobes intensity becomes weaker at Δx = 20 μm compared to the air scatterer at the same traveling distance. As the beam gradually propagates and reconstructs itself, the intensity of the main lobe recovers, as can be seen at Δx = 30 μm in Figure 3f. In fact, among the three different propagation lengths, the main lobe at Δx = 30 μm carries the most power. The recovery of the beam shape and power in the main lobe is sign of complete self-healing of the Airy-like beam. On the contrary, the Gaussian beam has completely decayed and lost its shape at the same propagation distance (Figure 3c). Note that the self-healing here is mainly referring to the self-healing of the main lobe. We do notice some discrepancies in the relative intensity of the side lobes between Figure 2 and Figure 3 and the profile after reconstruction does not exactly match the unscattered profile. However, it is the reconstruction of the main lobe that is the most important in practical applications, because most of the energy are concentrated in the main lobe.

In Table 1, we calculate the absolute values of Pearson correlation coefficients[28] between the scattered and unscattered Gaussian/accelerating beams to quantitively analyze the self-healing behavior (see also Figure S4 in the Supporting Information for a graphical analysis). Pearson correlation coefficients measure the linear correlation between two sets of data X and Y and have values from −1 to 1. Zero indicates no linear correlation at all, while ±1 implies that a linear equation describes the relationship between X and Y perfectly. Hence, the closer the coefficient's absolute value to unity, the stronger the association between the two data sets. Here, X is the unperturbed beam profile shown in Figure 2 and Y is the perturbed beam profile shown in Figure 3. At Δx = 10 μm, both Gaussian and Airy-like beams in the presence of scatterer correlate poorly with the unperturbed beams, indicating a large disparity between their profiles. At Δx = 20 μm, the scattered Gaussian beam matches the unperturbed Gaussian beam profile almost perfectly with a correlation coefficient as high as 0.97. This is due to the insufficient blocking of the light as shown in the simulation (Figure 3a). On the other hand, the correlation of scattered Airy-like beam remains to be near zero as self-healing is incomplete. At Δx = 30 μm, since there is no self-healing, the scattered Gaussian beam deviates significantly from the unperturbed beam as its correlation coefficient drops to 0.43 for air pocket and 0.33 for Al scatterer. In contrast, thanks to the self-reconstruction, the correlation coefficient of Airy-like beam increases dramatically to 0.84 for air pocket and 0.77 for Al scatterer as the scattered beam almost resembles the unperturbed beam (see Figure S3 in Supporting Information). The less-than-unity value of the correlations implies that there is some mismatch between the beam profiles, which mainly originate from the discrepancy in the side lobe intensity instead of the main lobe.

Table 1. Calculated Absolute Values of Pearson Correlation Coefficients at λ = 1541 nm between the Experimentally Measured Unscattered and Scattered Beam Profiles

Δx (μm)	Gaussian, air	Gaussian, Al	Airy, air	Airy, Al
10	0.26	0.27	0.02	0.00
20	0.97	0.96	0.08	0.01
30	0.43	0.33	0.84	0.77

Finally, it should be pointed out that the experimental data deviates more significantly from the simulation when the Al scatterer is used. This can be attributed to the nonideal packing of thermally evaporated Al inside the air pocket. From the SEM characterization, we found that the lift-off of Al results in a truncated cone, instead of a perfect cylinder, due to the shadowing effect of evaporation. Hence, some light is still able to penetrate the scatterer, producing a mixed scattering pattern. Despite this, the Al scatterer sufficiently attenuates the light more than air to allow the revelation of self-healing.

We further explore the self-healing of the side lobes in an Airy-like beam. A rectangular air slot 1 μm × 2 μm (centered at Δx = 12.2 μm, y = 2 μm) is used to block the side lobes of the 1D accelerating beam (Figure 4a). It can be clearly seen that the side lobes disappear in the shadow region behind the rectangular slot but starts to recover at Δx = 15.5 μm. At Δx = 20.5 μm, multiple side lobes have recovered their original intensity. Similar to the self-healing of the main lobe, the side lobes can self-heal, because the rays from the unblocked main lobe evolve into side lobes as they propagate. The simulation is corroborated by the experiments (Figure 4b). Note that the main peak of the Airy-like beam is unaffected as the scatterer is placed off-center. Near the air slot, the side lobes are completely suppressed (top plot, Figure 4b). From Δx = 15.5−20.5 μm, the primary side peak near y = 1.5 μm gradually reforms, matching the prediction of the simulation.

Finally, we show broadband operation across the telecommunication C-band with the synthetic-phase meta-optics. To understand the origin of the broadband behavior, it is essential to first analyze how the depth of focus and focal length of a 1D metalens is influenced by the chromatic dispersion. To begin with, the depth of focus of an ordinary lens with width w and focal length f is given by[29]

$$\Delta f = 4\lambda\frac{f^2}{w^2}$$

For a 1D metalens of 16 μm width and focal length of 15 μm operating at 1550 nm, the depth of focus is calculated to be ∼5.45 μm. Such depth of focus can be further increased by designing a smaller diameter lens with long focal length. Meanwhile, the focal length shift of a 1D metalens from wavelength variation originates from the fixed $\phi(\lambda) = \frac{2\pi}{\lambda}L$, imposed by length L of the air slot, if we assume the silicon is approximately dispersionless in the wavelength of interest. At a different wavelength λ_1, the phase imparts on the wavefront becomes $\phi(\lambda_1)$ instead of the designed phase $\phi(\lambda_0)$. At the locations where phase wrapping occurs, L changes abruptly and hence $\phi(\lambda_1)$ can no longer follow the ideal phase profile for λ_1 but approaches the phase profile $\phi(\lambda_0)$[30]. As a result, the focal length changes with the wavelength shift with an approximate relationship of $f \propto \frac{1}{\lambda}$. We estimate that the

https://doi.org/10.1021/acsphotonics.1c00581
ACS Photonics XXXX, XXX, XXX−XXX

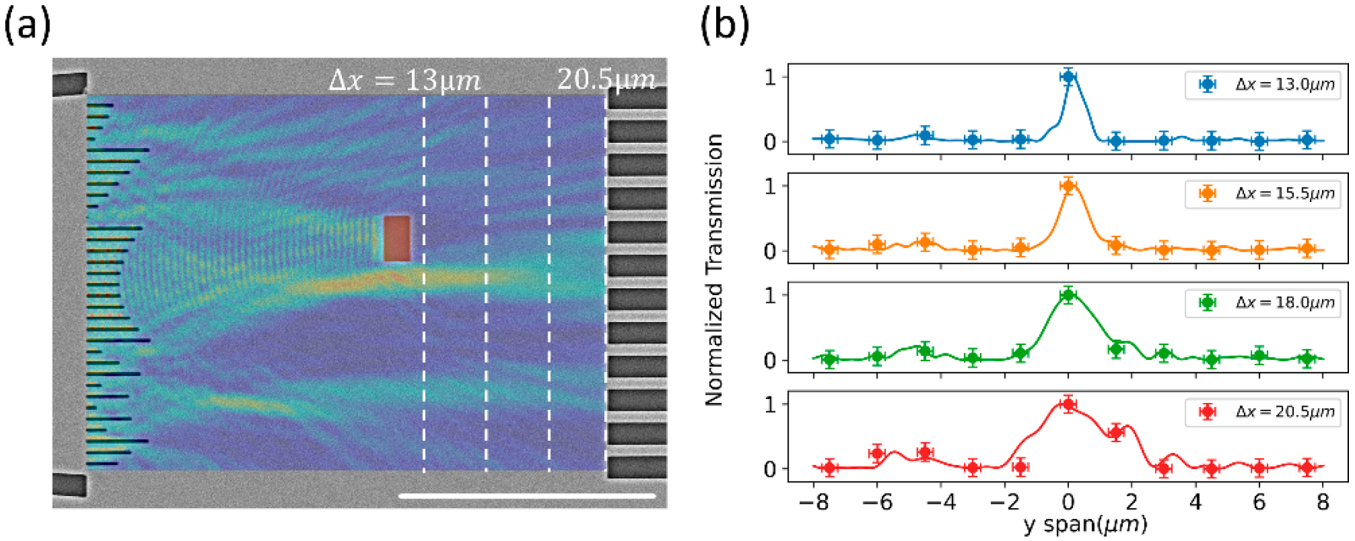

Figure 4. Self-healing of on-chip 1D accelerating beam side lobes. (a) SEM of the synthetic-phase meta-optic and the rectangular air scatterer (scale bar: 10 μm). The scatterer is highlighted with false color and the simulated electric field distribution is overlapped onto the SEM image. The white dashed lines indicate where the optical transmission is measured. (b) Intensity distribution across the y span showing the self-healing of Airy-like beam side peaks. Solid lines are the simulation results and dots are the measured data in experiment measured at each waveguide. Error bars in x are determined by the lateral span of the intensity point which equals to the 500 nm waveguide width. Error bars in y are calculated from the standard deviation of grating coupler efficiency across the whole chip.

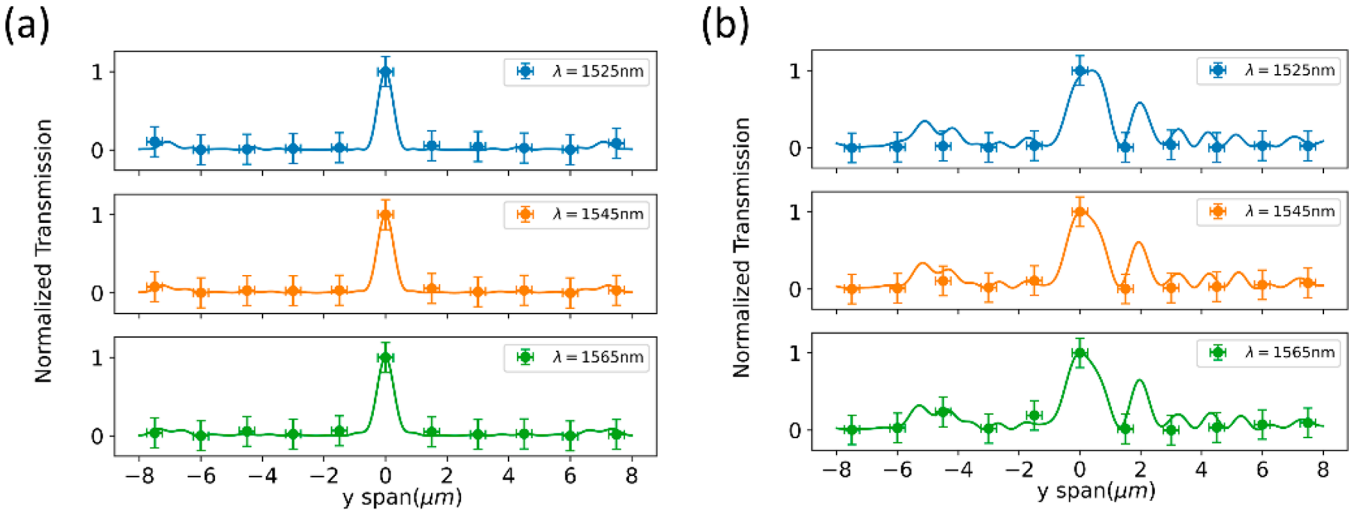

Figure 5. Broadband operation of synthetic-phase meta-optics across the C-band. (a) Gaussian beam profile formed by a quadratic metalens measured at Δx = 15 μm across the telecommunication C-band. (b) 1D Airy-like beam profile measured at Δx = 15 μm across the telecommunication C-band. Solid lines are the simulation results and dots are the measured data in experiment at each waveguide. Error bars in x are determined by the lateral span of the intensity point which equals to the 500 nm waveguide width. Error bars in y are calculated from the standard deviation of grating coupler efficiency across the whole chip.

focal length changes from 15.28 μm at 1525 nm to 15.08 μm at 1545 nm. This focal length change of 0.2 μm is far less than the calculated depth of focus of 5.45 μm, which means the Gaussian beam remains tightly focused despite the wavelength shift and the metalens is fundamentally broadband in the telecom C-band. This is experimentally verified, accompanied by FDTD simulation in Figure 5c (measured at Δx = 15 μm). Such broadband behavior has also been reported in simulation and experiment before.[24,31]

Figures 1 and 2 have already shown that the addition of cubic phase can extend the depth of focus of a metalens, which makes the focal length drift due to dispersion even less noticeable. This is confirmed in Figure 5b. Although the synthetic-phase meta-optic is designed to operate at 1550 nm, varying the center wavelength does not affect its performance. The 1D Airy-like beam profile (measured at Δx = 15 μm) originated from the same meta-optics remains relatively unchanged across the telecom C-band and the main lobe does not diverge significantly thanks to its EDOF. We note that, however, the EDOF further increases the bandwidth of the cubic meta-optics and ultimately the operation bandwidth will only be limited by the grating coupler efficiencies. Similar broadband behavior has also been reported recently in the 2D Airy beam generated from synthetic-phase metasurface in the visible.[20]

https://doi.org/10.1021/acsphotonics.1c00581
ACS Photonics XXXX, XXX, XXX−XXX

DISCUSSION

We should point out that the on-chip accelerating beam is not intended for strong light enhancement. Optical cavities such as microring resonators and photonic crystals can provide much stronger light enhancement in integrated photonics than focused Gaussian beam and Airy beam. However, the light concentration provided by the photonic cavities is very localized and the spatial position of the confined mode is generally not tunable. This will be undesirable for applications such as particle manipulation[10] and light routing on chip[21] where a spatially tunable elongated beam is preferred. A 1D accelerating beam will be attractive in this case as it has an elongated spatial extent thanks to its nondiffracting nature. Additionally, photonic cavities are narrow band, as light enhancement only occurs at the resonant wavelength. In contrast, the light concentration of the accelerating beam is very broadband because it is not a resonance effect.

We would like to further justify the use of the Pearson correlation to quantify the self-healing behavior of the accelerating beam. In general, the Pearson correlation function measures how similar two vectors are. While this measure is often used for random signals, it can also be used for a deterministic signal. In this case, the two variables, scattered and unscattered beam profiles, are two different vectors, and the Pearson correlation coefficient measures how similar they are. When the coefficient value is close to ± 1, then there exists a linear relation between two vectors. If two vectors are identical (except for a scaling factor), then the absolute value of the correlation becomes unity. Hence, if the optical beam becomes completely random, for example, when passing through a random scatterer array, we expect the coefficient to be zero. A Gaussian beam after perturbation will still have correlation with the unperturbed beam but this correlation will be weak, see Figure S4c,d. As such the correlation value corresponds to the similarity between two vectors.

The limited resolution of data sampling is constrained by minimum waveguide spacing between the output ports to avoid coupling between the waveguides. To further improve the resolution, the output waveguides can fan out,[32] as opposed to being parallel to each other (as shown in Figure 1d). However, this method will lead to a very large device area. As we have mentioned previously, the larger the device area, the greater the variation in the grating coupler efficiency and hence the larger the errors. Alternatively, a scanning probe method could be used to obtain a high resolution near-field beam profile.[33] However, the technique only detects the evanescent field from the waveguide and, hence, has a poor signal-to-noise ratio, particularly at the low intensity side lobes. Additionally, the signal can be further obscured by the light scattered upward by the scatterers. Whereas in our approach, the light is detected through a wave confined structure and only the in-plane intensity is collected. Hence, our approach is expected to have a larger signal-to-noise ratio than detecting the evanescent wave. Another potential solution is to use a foundry process that allows less nonuniformity and variation in etching within a large area. In this way, more grating couplers can be used to collect more data points. Nevertheless, the main goal of this paper is to show the nondiffraction and self-healing behavior of the accelerating beams, which are supported by our findings. Obtaining a high-resolution image of the 1D Airy beam will constitute a future goal.

CONCLUSION

In conclusion, we have demonstrated for the first time the formation of self-healing and nondiffracting accelerating beam in a waveguiding structure using silicon integrated photonics. It should be pointed out that such a 1D accelerating beam is not dependent on the material platform being used. Any planar waveguides can be designed to support the propagation of 1D accelerating beam across different wavelengths of interest. For example, recently a broadband 1D metalens has been designed on Al_2O_3 platform for operation in the visible wavelength.[31] The nondiffracting and self-healing nature of the 1D Airy-like beam makes it particularly attractive for operation in turbulent and scattering media such as a fluid. Hence, the 1D accelerating beam could possibly be generated in optofluidic waveguides[34] for applications such as microfluidic flow cytometry[22,35] and cell sorting.[36] Enhanced sensing resolution is expected since the 1D Airy beam has a narrower main lobe fwhm (1 μm) and suffers from less diffraction compared to the beam generated by a nanoantenna.[22] In this case, the meta-optics will be implemented by silicon scatterers, because the biomolecules cannot flow in the silicon waveguides, and the 1D Airy beam will propagate freely in the fluid. Additionally, the methodology we present here is universal, and hence, other classes of nondiffracting beams, such as the Bessel beam,[33] can also be generated by tailoring the phase mask design. Finally, reconfigurability can be explored in the future using integrated metallic heaters[22] or phase-change materials[37,38] for beam steering and focal length tuning of the 1D self-healing beam, which can potentially act as an ultracompact $1 \times N$ optical switch for on-chip light routing in optical interconnects. An Airy beam will be more suited for such applications than a Gaussian beam, as it suffers from minimal diffraction and self-heals when disturbed by fabrication imperfections.

METHODS

SOI Device Fabrication. The 1D meta-optics were fabricated on a 220 nm thick silicon layer on top of a 3 μm thick buried oxide layer (SOITECH). The pattern was defined by a JEOLJBX-6300FS 100 kV electron-beam lithography (EBL) system using positive tone ZEP-520A resist. The 220 nm fully etched ridge waveguides, meta-optics, and air scatterers were made by an inductively coupled plasma reactive ion etching (ICP-RIE) process. A second EBL exposure using positive tone poly(methyl methacrylate) (PMMA) resist was subsequently carried out to create windows for the Al deposition. After development, 220 nm Al was electron beam evaporated onto the chip. The lift-off of Al was completed using methylene chloride.

Experimental Setup. The meta-optics on SOI were characterized by a vertical fiber-coupling setup.[37] All the measurements were performed under ambient conditions, while the temperature of the stage was fixed at ~24 °C by a thermoelectric controller (TEC, TE Technology TC-720). The input light was provided by a tunable continuous-wave laser (Santec TSL-510), and its polarization was controlled by a manual fiber polarization controller (Thorlabs FPC526) to match the fundamental quasi-TE mode of the waveguides. A low-noise power meter (Keysight 81634B) was used to collect the static optical output from the grating couplers.

https://doi.org/10.1021/acsphotonics.1c00581
ACS Photonics XXXX, XXX, XXX−XXX

■ ASSOCIATED CONTENT

Supporting Information

The Supporting Information is available free of charge at https://pubs.acs.org/doi/10.1021/acsphotonics.1c00581.

Figure S1: Influence of alpha on the 1D Airy-like beam; Figure S2: Variation of the beam width with the propagation distance; Figure S3: Comparison between the perturbed and unperturbed beam profile; Figure S4: Graphical analysis of Pearson correlation (PDF)

■ AUTHOR INFORMATION

Corresponding Authors

Zhuoran Fang − *Department of Electrical and Computer Engineering, University of Washington, Seattle, Washington 98195, United States;* orcid.org/0000-0001-8724-6633; Email: rogefzr@uw.edu

Arka Majumdar − *Department of Electrical and Computer Engineering and Department of Physics, University of Washington, Seattle, Washington 98195, United States;* orcid.org/0000-0003-0917-590X; Email: arka@uw.edu

Authors

Rui Chen − *Department of Electrical and Computer Engineering, University of Washington, Seattle, Washington 98195, United States*

Albert Ryou − *Department of Electrical and Computer Engineering, University of Washington, Seattle, Washington 98195, United States*

Complete contact information is available at: https://pubs.acs.org/10.1021/acsphotonics.1c00581

Author Contributions

Z.F. and A.M. conceived the project. Z.F. simulated, designed, and fabricated the devices. Z.F. performed the experiments. R.C. helped with the experiments and simulations. A.R. helped with the simulation. A.M. supervised the overall progress of the project. Z.F. wrote the manuscript with input from all the authors.

Funding

National Science Foundation (NSF-2003509), ONR-YIP Award, and Washington Research Foundation.

Notes

The authors declare no competing financial interest.

■ ACKNOWLEDGMENTS

Part of this work was conducted at the Washington Nanofabrication Facility/Molecular Analysis Facility, a National Nanotechnology Coordinated Infrastructure (NNCI) site at the University of Washington, which is supported in part by funds from the National Science Foundation (Awards NNCI-1542101, 1337840, and 0335765), the National Institutes of Health, the Molecular Engineering and Sciences Institute, the Clean Energy Institute, the Washington Research Foundation, the M. J. Murdock Charitable Trust, Altatech, ClassOne Technology, GCE Market, Google, and SPTS.

■ REFERENCES

(1) McGloin, D.; Dholakia, K. Bessel Beams: Diffraction in a New Light. *Contemp. Phys.* **2005**, *46* (1), 15−28.

(2) Siviloglou, G. A.; Broky, J.; Dogariu, A.; Christodoulides, D. N. Observation of Accelerating Airy Beams. *Phys. Rev. Lett.* **2007**, *99* (21), 213901.

(3) Efremidis, N. K.; Chen, Z.; Segev, M.; Christodoulides, D. N. Airy Beams and Accelerating Waves: An Overview of Recent Advances. *Optica, OPTICA* **2019**, *6* (5), 686−701.

(4) Siviloglou, G. A.; Christodoulides, D. N. Accelerating Finite Energy Airy Beams. *Opt. Lett.* **2007**, *32* (8), 979−981.

(5) Voloch-Bloch, N.; Lereah, Y.; Lilach, Y.; Gover, A.; Arie, A. Generation of Electron Airy Beams. *Nature* **2013**, *494* (7437), 331−335.

(6) Zhang, P.; Wang, S.; Liu, Y.; Yin, X.; Lu, C.; Chen, Z.; Zhang, X. Plasmonic Airy Beams with Dynamically Controlled Trajectories. *Opt. Lett.* **2011**, *36* (16), 3191.

(7) Broky, J.; Siviloglou, G. A.; Dogariu, A.; Christodoulides, D. N. Self-Healing Properties of Optical Airy Beams. *Opt. Express* **2008**, *16* (17), 12880−12891.

(8) Jia, S.; Vaughan, J. C.; Zhuang, X. Isotropic Three-Dimensional Super-Resolution Imaging with a Self-Bending Point Spread Function. *Nat. Photonics* **2014**, *8* (4), 302−306.

(9) Vettenburg, T.; Dalgarno, H. I. C.; Nylk, J.; Coll-Lladó, C.; Ferrier, D. E. K.; Čižmár, T.; Gunn-Moore, F. J.; Dholakia, K. Light-Sheet Microscopy Using an Airy Beam. *Nat. Methods* **2014**, *11* (5), 541−544.

(10) Baumgartl, J.; Mazilu, M.; Dholakia, K. Optically Mediated Particle Clearing Using Airy Wavepackets. *Nat. Photonics* **2008**, *2* (11), 675−678.

(11) Baumgartl, J.; Hannappel, G. M.; Stevenson, D. J.; Day, D.; Gu, M.; Dholakia, K. Optical Redistribution of Microparticles and Cells between Microwells. *Lab Chip* **2009**, *9* (10), 1334−1336.

(12) Zheng, Z.; Zhang, B.-F.; Chen, H.; Ding, J.; Wang, H.-T. Optical Trapping with Focused Airy Beams. *Appl. Opt.* **2011**, *50* (1), 43−49.

(13) Mathis, A.; Courvoisier, F.; Froehly, L.; Furfaro, L.; Jacquot, M.; Lacourt, P. A.; Dudley, J. M. Micromachining along a Curve: Femtosecond Laser Micromachining of Curved Profiles in Diamond and Silicon Using Accelerating Beams. *Appl. Phys. Lett.* **2012**, *101* (7), 071110.

(14) Götte, N.; Winkler, T.; Meinl, T.; Kusserow, T.; Zielinski, B.; Sarpe, C.; Senftleben, A.; Hillmer, H.; Baumert, T. Temporal Airy Pulses for Controlled High Aspect Ratio Nanomachining of Dielectrics. *Optica, OPTICA* **2016**, *3* (4), 389−395.

(15) Polynkin, P.; Kolesik, M.; Moloney, J. V.; Siviloglou, G. A.; Christodoulides, D. N. Curved Plasma Channel Generation Using Ultraintense Airy Beams. *Science* **2009**, *324* (5924), 229−232.

(16) Liu, K.; Koulouklidis, A. D.; Papazoglou, D. G.; Tzortzakis, S.; Zhang, X.-C. Enhanced Terahertz Wave Emission from Air-Plasma Tailored by Abruptly Autofocusing Laser Beams. *Optica, OPTICA* **2016**, *3* (6), 605−608.

(17) Cottrell, D. M.; Davis, J. A.; Hazard, T. M. Direct Generation of Accelerating Airy Beams Using a 3/2 Phase-Only Pattern. *Opt. Lett.* **2009**, *34* (17), 2634−2636.

(18) Greenfield, E.; Segev, M.; Walasik, W.; Raz, O. Accelerating Light Beams along Arbitrary Convex Trajectories. *Phys. Rev. Lett.* **2011**, *106* (21), 213902.

(19) Froehly, L.; Courvoisier, F.; Mathis, A.; Jacquot, M.; Furfaro, L.; Giust, R.; Lacourt, P. A.; Dudley, J. M. Arbitrary Accelerating Micron-Scale Caustic Beams in Two and Three Dimensions. *Opt. Express* **2011**, *19* (17), 16455−16465.

(20) Wen, J.; Chen, L.; Yu, B.; Nieder, J. B.; Zhuang, S.; Zhang, D.; Lei, D. All-Dielectric Synthetic-Phase Metasurfaces Generating Practical Airy Beams. *ACS Nano* **2021**, *15* (1), 1030−1038.

(21) Rose, P.; Diebel, F.; Boguslawski, M.; Denz, C. Airy Beam Induced Optical Routing. *Appl. Phys. Lett.* **2013**, *102* (10), 101101.

(22) García-Meca, C.; Lechago, S.; Brimont, A.; Griol, A.; Mas, S.; Sánchez, L.; Bellieres, L.; Losilla, N. S.; Martí, J. On-Chip Wireless Silicon Photonics: From Reconfigurable Interconnects to Lab-on-Chip Devices. *Light: Sci. Appl.* **2017**, *6* (9), No. e17053.

(23) Yu, S.; Lu, J.; Ginis, V.; Kheifets, S.; Lim, S. W. D.; Qiu, M.; Gu, T.; Hu, J.; Capasso, F. On-Chip Optical Tweezers Based on Freeform Optics. *Optica* **2021**, *8* (3), 409−414.

(24) Wang, Z.; Li, T.; Soman, A.; Mao, D.; Kananen, T.; Gu, T. On-Chip Wavefront Shaping with Dielectric Metasurface. *Nat. Commun.* **2019**, *10* (1), na DOI: 10.1038/s41467-019-11578-y.
(25) Zhan, A.; Colburn, S.; Dodson, C. M.; Majumdar, A. Metasurface Freeform Nanophotonics. *Sci. Rep.* **2017**, *7* (1), 1673.
(26) Colburn, S.; Zhan, A.; Majumdar, A. Metasurface Optics for Full-Color Computational Imaging. *Science Advances* **2018**, *4* (2), No. eaar2114.
(27) Bandres, M. A.; Kaminer, I.; Mills, M.; Rodríguez-Lara, B. M.; Greenfield, E.; Segev, M.; Christodoulides, D. N. Accelerating Optical Beams. *Opt. Photonics News* **2013**, *24* (6), 30−37.
(28) Pearson Correlation Coefficient. https://en.wikipedia.org/wiki/Pearson_correlation_coefficient; accessed 2021.
(29) Bayati, E.; Pestourie, R.; Colburn, S.; Lin, Z.; Johnson, S. G.; Majumdar, A. Inverse Designed Metalenses with Extended Depth of Focus. *ACS Photonics* **2020**, *7* (4), 873−878.
(30) Arbabi, E.; Arbabi, A.; Kamali, S. M.; Horie, Y.; Faraon, A. Multiwavelength Polarization-Insensitive Lenses Based on Dielectric Metasurfaces with Meta-Molecules. *Optica, OPTICA* **2016**, *3* (6), 628−633.
(31) Yang, R.; Shi, Y.; Dai, C.; Wan, C.; Wan, S.; Li, Z. On-Chip Metalenses Based on One-Dimensional Gradient Trench in the Broadband Visible. *Opt. Lett.* **2020**, *45* (20), 5640−5643.
(32) Liao, K.; Gan, T.; Hu, X.; Gong, Q. AI-Assisted on-Chip Nanophotonic Convolver Based on Silicon Metasurface. *Nanophotonics* **2020**, *9* (10), 3315−3322.
(33) Fan, Y.; Cluzel, B.; Petit, M.; Le Roux, X.; Lupu, A.; de Lustrac, A. 2D Waveguided Bessel Beam Generated Using Integrated Metasurface-Based Plasmonic Axicon. *ACS Appl. Mater. Interfaces* **2020**, *12* (18), 21114−21119.
(34) Schmidt, H.; Hawkins, A. R. The Photonic Integration of Non-Solid Media Using Optofluidics. *Nat. Photonics* **2011**, *5* (10), 598−604.
(35) Mao, X.; Lin, S.-C. S.; Lapsley, M. I.; Shi, J.; Juluri, B. K.; Huang, T. J. Tunable Liquid Gradient Refractive Index (L-GRIN) Lens with Two Degrees of Freedom. *Lab Chip* **2009**, *9* (14), 2050−2058.
(36) Wang, X.; Chen, S.; Kong, M.; Wang, Z.; Costa, K. D.; Li, R. A.; Sun, D. Enhanced Cell Sorting and Manipulation with Combined Optical Tweezer and Microfluidic Chip Technologies. *Lab Chip* **2011**, *11* (21), 3656−3662.
(37) Zheng, J.; Fang, Z.; Wu, C.; Zhu, S.; Xu, P.; Doylend, J. K.; Deshmukh, S.; Pop, E.; Dunham, S.; Li, M.; Majumdar, A. Nonvolatile Electrically Reconfigurable Integrated Photonic Switch Enabled by a Silicon PIN Diode Heater. *Adv. Mater.* **2020**, *32* (31), 2001218.
(38) Fang, Z.; Zheng, J.; Saxena, A.; Whitehead, J.; Chen, Y.; Majumdar, A. Non-Volatile Reconfigurable Integrated Photonics Enabled by Broadband Low-Loss Phase Change Material. *Adv. Opt. Mater.* **2021**, *9* (9), 2002049.

https://doi.org/10.1021/acsphotonics.1c00581
ACS Photonics XXXX, XXX, XXX−XXX